

# Compensation for Aberrations of Focused Ultrasound Beams in Transcranial Sonications of Brain at Different Depths

D. D. Chupova<sup>a, \*</sup>, P. B. Rosnitskiy<sup>a</sup>, L. R. Gavrilov<sup>b, \*\*</sup>, and V. A. Khokhlova<sup>a</sup>

<sup>a</sup> Lomonosov Moscow State University, Moscow, 119991 Russia

<sup>b</sup> Andreyev Acoustics Institute, Moscow, 117036 Russia

\*e-mail: [daria.chupova@yandex.ru](mailto:daria.chupova@yandex.ru)

\*\*e-mail: [lrgavrilov.1938@mail.ru](mailto:lrgavrilov.1938@mail.ru)

Received August 27, 2021; revised September 21, 2021; accepted September 22, 2021

**Abstract**—The study analyzes the possibilities of compensating for aberrations when focusing an ultrasound beam through the skull bones using arrays with mosaic pattern of elements, curvature radius and aperture of  $F = D = 200$  mm, frequency of 1 MHz, and fully populated randomized pattern of the elements. The effect of the number of elements (256, 512, and 1024) and focusing depth (25–65 mm from the inner surface of the skull) on the quality of aberration correction is considered, i.e., the sharpness of focusing, location of the focus, and the maximum pressure therein. An acoustic model of the human head is constructed from magnetic resonance imaging (MRI) data. The field and compensation for aberrations are calculated using the Rayleigh integral and wave equation in the Kelvin–Voigt model. The possibility of sharp focusing with the focal region width of about 2 mm at the level of 6 dB using the considered arrays is demonstrated within the indicated depth interval. The relative contribution of different wave effects to distortion of the ultrasound beam as it passes through the skull is analyzed. It is shown that the strongest contributions to beam attenuation come from aberrations (7.4 dB) and absorption (6.7 dB). Contributions from reflection (2.1 dB) and shear-wave generation in the skull (2 dB) are less significant.

**Keywords:** medical acoustics, high intensity focused ultrasound (HIFU), multi-element arrays, Rayleigh integral

**DOI:** 10.1134/S1063771022010018

## INTRODUCTION

The use of high intensity focused ultrasound (HIFU) to treat brain pathologies is currently one of the most successful clinical trends in noninvasive ultrasound surgery [1–6]. By focusing the ultrasound beam through the bones of the skull into target areas of the brain, thermal ablation is realized inside the predetermined pathological areas by rapid localized heating. Such treatments, performed without direct surgical intervention, significantly reduce the risks of infection and damage to healthy brain tissues [7]. However, skull bones distort the spatial structure of the ultrasound beam; therefore, for aberration correction and ensuring sharp ultrasound focusing, multi-element phased arrays are used, which enable independent variation of the amplitude and phase on each array element [7, 8]. To determine the required phases at the elements, both ray [9] and diffraction methods based on time reversal [10] or phase conjugation [11] are applied. In neurosurgical practice, 1024-element arrays of ExAblate clinical systems (InSightec Ltd., Tirat Carmel, Israel) are successfully used. The arrays have the shape of a hemisphere with a radius of curva-

ture of 150 mm, an aperture of 300 mm, and an operating frequency of 650–720 kHz [8]. Such array configuration allows for irradiating the central regions of the brain in the thalamus area and for treating essential tremor, the tremor caused by Parkinson’s disease, localized tumors, and other brain diseases [1–6]. In the literature known to us, no quantitative data have been provided on the size of the possible focus steering area for these cases.

Recently, a new class of multi-element arrays was proposed with a more compact form: the segment of a sphere with a convergence angle  $\alpha = 2 \arcsin(D/2F) = 60^\circ$ , curvature and aperture radius  $F = D = 200$  mm, and higher operating frequency  $f = 1$  MHz. The active area of the array and, accordingly, radiated power is approximately half of that of a hemispherical array; however, this power deficit can be partially compensated by fully populated randomized filling of the array surface with mosaic structure of the elements (Fig. 1a) [12–14]. Note that several designs of therapeutic arrays with similar convergence angles and mosaic elements pattern have been proposed by other authors, but these designs did not yield the maximum achiev-

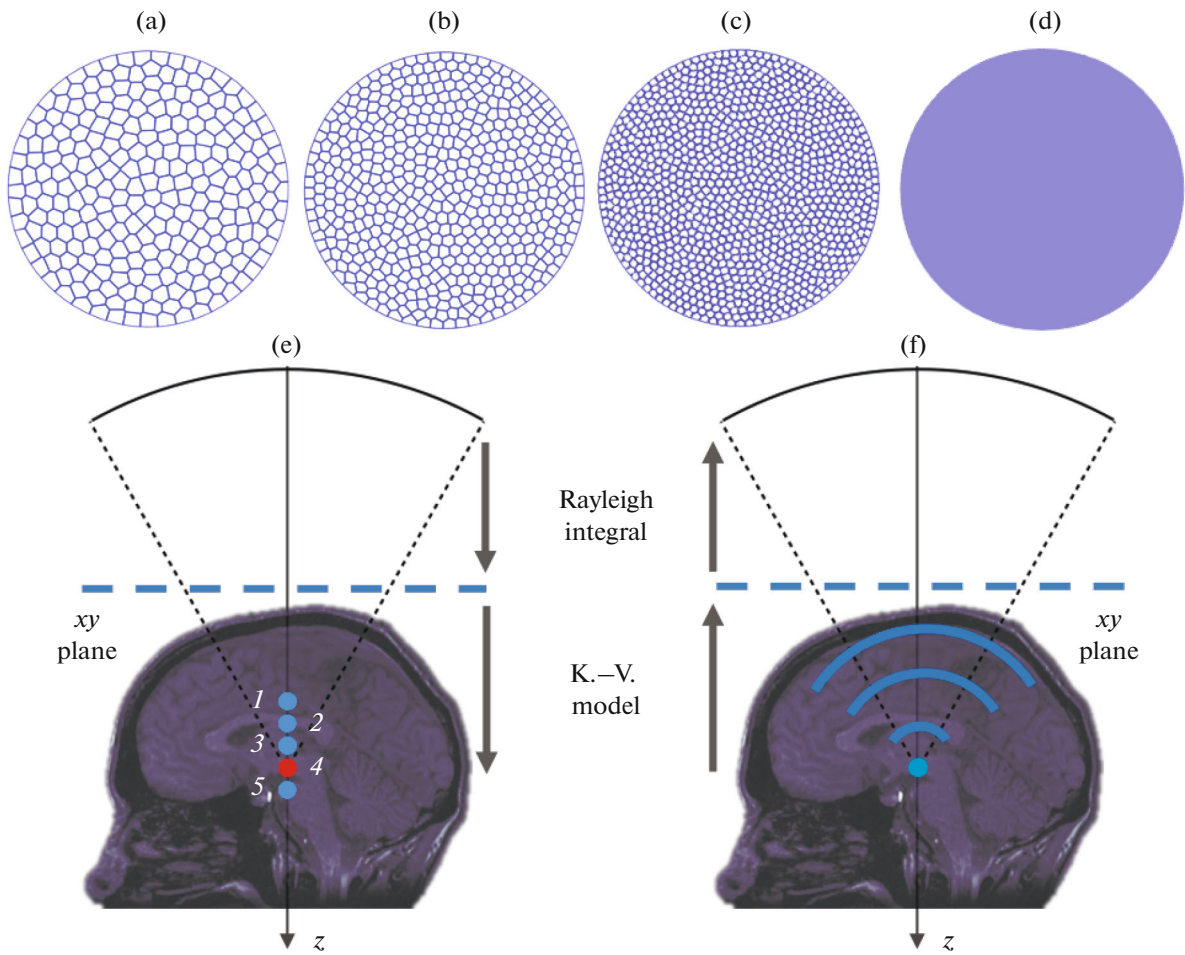


**Fig. 1.** Sketches of the studied arrays: (a) 256 elements, (b) 512 elements, (c) 1024 elements, (d) idealized array. (e) Illustration of methods for calculating ultrasound field for sonications in brain and (f) aberration compensation. Arrows show the order of calculations: with Rayleigh integral and Kelvin–Voigt (K.–V.) model. Array focus was positioned at different depths (e): array center of curvature was relocated relative to center of brain by  $-30$  (1),  $-20$  (2),  $-10$  (3),  $0$  (4),  $+10$  mm (5).

able area of the active surface, which was realized in the fully populated pattern used in this study [15, 16].

The compact shape and relatively small convergence angle of the array allow for its rotation and translation relative to the patient's head without significant change in the beam's angle of incidence on the skull. On the contrary, relocation of the existing hemispherical arrays changes the angle of wave's incidence on the skull that results in significant energy losses. The area of possible mechanical focus steering is also limited for hemispherical arrays due to their geometry and positioning relative to the human head. Thus, the model considered in this study can potentially enlarge the area of mechanical focus steering around the center of the brain without creating additional diffraction maxima in the acoustic field and thus enlarge currently achievable spatial region of brain tissue for effective and safe insonation.

In addition, our earlier works theoretically showed that using such an array with 1 MHz frequency,

256 elements, and compensation for skull-induced aberrations, it is possible to achieve the pressures sufficient to form high-amplitude shock fronts at the focus and mechanically destroy tissues via boiling histotripsy method [12, 13]. This method is practically free of thermal effects, which reduces the risk of overheating the skull [17–19]. However, for arrays with different numbers of elements and brain regions outside the thalamus, aberration correction studies have not been carried out even in the approximation of linear focusing of the beam through the skull bones.

The goal of this work was to investigate theoretically how the number of elements in the proposed arrays and the depth of focusing in the brain during mechanical relocation of the array affect the quality of aberration correction in a focused linear beam. The main criteria for assessing the quality of aberration compensation were considered as the sharpness of focusing (width and length of the focal peak), correct location of the focus, and the level of maximum pres-

**Table 1.** Values of compressional  $c_l$  and shear  $c_s$  sound speeds, density  $\rho_0$ , and absorption coefficients of compressional  $\alpha_l$  and shear  $\alpha_s$  waves for water, skin, skull, and brain

	$c_l$ , m/s	$c_s$ , m/s	$\rho_0$ , kg/m <sup>3</sup>	$\alpha_l$ , dB/cm	$\alpha_s$ , dB/cm
Water	1500	0	1000	0	0
Skin	1624	0	1109	1.84	0
Skull	2820	1500	1732	8.83	19.15
Brain	1550	0	1030	0.21	0

sure therein. Relative contribution of different wave effects to distortion of the beam structure and maximum attainable wave amplitude were evaluated. The effects of shear-wave generation in the skull, absorption, reflection, and aberrations arising as the beam passes through nonuniformly thick skull bones, were considered. In numerical experiment, an acoustic model of the human head, constructed from magnetic resonance imaging (MRI) data, was employed. The array field and aberration compensation were calculated by an earlier developed method that combines different wave models [12].

### THEORETICAL MODEL

Consider a model of a multi-element array in a shape of a spherical segment with a focal length and aperture  $F = D = 200$  mm, convergence angle  $60^\circ$ , and operating frequency  $f = 1$  MHz [13]. Using a previously developed algorithm for generating a mosaic pattern of equal area cells, the array surface was divided into elements in the shape of polygons randomly distributed on the array surface providing absolutely dense filling of the transducer surface with elements [14]. Such partitioning method simultaneously maximizes the active area of an array with a given geometry and minimizes unwanted diffraction effects caused by periodic arrangement of elements [20]. For technical implementation of the transducer model, a gap of 0.5 mm between the elements was introduced. The developed algorithm made it possible to construct array models with different numbers of elements: 256, 512, and 1024 (Figs. 1a–1c). The filling factor of the arrays, taking into account the gap between elements, was 92% (element area 121 mm<sup>2</sup>) for the 256-element array, 88% (element area 58 mm<sup>2</sup>) for the 512-element array, and 84% (element area 28 mm<sup>2</sup>) for the 1024-element array. An idealized array model with a conditionally infinite number of elements (Fig. 1d) was also considered. To construct such an array, a computational rectangular mesh was projected onto the spherical surface of the transducer providing the possibility to quasi-continuously vary the amplitude and phase on the transducer surface [21].

To simulate focusing of the ultrasound beam through an intact skull, a three-dimensional acoustic model of the human head, constructed from MRI

data, was used [12]. The head model was represented by a set of 91 axial images,  $191 \times 256$  pixels each, taken at different heights. The spatial resolution of the images was  $1 \times 1 \times 1$  mm. Each image was divided by thresholding method into four segments: water-filled outer space, skin, skull, and brain. The model took into account the geometric features of each segment of the human head, while each medium was considered homogeneous [22, 23] with the following parameters [12]: density  $\rho_0$  [24], compressional sound speed  $c_l$  [25], absorption coefficient  $\alpha_l$  [24], as well as the shear wave sound speed  $c_s$  and absorption coefficient  $\alpha_s$  (nonzero only for the skull) [24, 25]. The parameters of all segments were set in the numerical algorithm in the form of a matrix with corresponding values given in Table 1.

The numerical algorithm for simulating ultrasound focusing consisted of two combined methods. At the first stage, the acoustic field of the transducer was calculated using the Rayleigh integral [26] in a homogeneous medium (water) from the surface of the array to the horizontal plane ( $xy$ ) near the surface of the skull (Fig. 1e):

$$p(\mathbf{r}) = -\frac{i\omega\rho_0}{2\pi} \int_S \frac{v_n(\mathbf{r}') \exp(ikR)}{R} dS', \quad (1)$$

where  $\omega = 2\pi f$  is the angular frequency,  $k = \omega/c_0$  is the wavenumber,  $c_0$  is the sound speed in the medium,  $\rho_0$  is the density of the medium,  $v_n(\mathbf{r}')$  is the complex amplitude of the vibrational velocity on the  $xy$  plane,  $\mathbf{r}'$  is the radius vector of a surface element  $dS'$ ,  $S$  is the area of the  $xy$  plane,  $R = |\mathbf{r} - \mathbf{r}'|$  is the distance from the element area  $dS'$  to the observation point with the coordinate  $\mathbf{r}$ . The time-dependent component of the complex field amplitude  $\exp(-i\omega t)$  was considered, where  $i$  is the imaginary unit. The vibrational velocity amplitude distribution on the surface of the elements was assumed to be uniform:  $v_n(\mathbf{r}') = v_0$ .

Direct numerical calculation of the Rayleigh integral (1) from the surface of the multi-element array is quite time consuming, especially for a series of calculations. For the considered array design, the distance between the transducer and the given plane significantly exceeds the near field of an array element;

therefore, to speed up calculations, an analytical method was used that calculates the acoustic field on the  $xy$  plane as the sum of analytical solutions for the far field of each array element [13, 14, 20]. To perform such calculations, the polygonal elements of the transducer were preliminarily divided into right triangles. In turn, the field of the triangular transducer was calculated by the formula [14]:

$$p = \frac{p_0 ab \exp(ikr_0)[I(a, x) - I(b, y)]}{2\pi r_0(ax/r_0 - by/r_0)}, \quad (2)$$

where  $I(a, x) = \exp(-ika/2(x/r_0)) \text{sinc}(ka/2(x/r_0))$ ,  $a$  and  $b$  are the legs of a right triangle,  $p_0 = \rho_0 c_0 v_n$  is the characteristic pressure on the element surface,  $r_0 = (x^2 + y^2 + z^2)^{1/2}$  is the radius vector of the observation point, and  $\{x, y, z\}$  are the coordinates of the observation point. Thus, the acoustic pressure field on the  $xy$  plane located perpendicular to the array axis near the surface of the skull, was found as the sum of the fields of the right-triangle sub-elements into which the transducer elements were divided.

The result obtained was used as a boundary condition for further calculation of the field near the human head. A numerical solution was obtained using the k-Wave software ([www.k-wave.org](http://www.k-wave.org)), which is based on the pseudospectral method for solving the wave equation in the Kelvin–Voigt model [22, 23]:

$$\begin{aligned} \rho_0 \frac{\partial^2 \mathbf{u}}{\partial t^2} &= (\lambda + \mu) \nabla(\nabla \cdot \mathbf{u}) + \mu \nabla^2 \mathbf{u} \\ &+ (\chi + \eta) \nabla \left( \nabla \cdot \frac{\partial \mathbf{u}}{\partial t} \right) + \eta \nabla^2 \frac{\partial \mathbf{u}}{\partial t}, \end{aligned} \quad (3)$$

where  $\mathbf{u}$  is the displacement of particles in the medium,  $\lambda$  and  $\mu$  are the Lamé parameters,  $\mu$ —shear modulus,  $\chi$  and  $\eta$ —compression and shear viscosity coefficients, respectively. The Lamé parameters are related to the compressional  $c_l$  and shear  $c_s$  sound speeds as follows:  $c_s^2 = \mu/\rho_0$ ,  $c_l^2 = (\lambda + 2\mu)/\rho_0$ ; the absorption coefficients  $\alpha_s$  and  $\alpha_l$  are related to the viscosity coefficients:  $\alpha_s = \eta\omega^2/(2\rho_0 c_s^3)$  and  $\alpha_l = (\chi + 2\eta)\omega^2/(2\rho_0 c_l^3)$ .

This model (3) takes into account the effects of diffraction, absorption, inhomogeneities, and shear-wave generation in the skull. As a result of combining the methods (2) and (3), the acoustic pressure amplitude distribution ( $p_A/p_0$ ) normalized to the characteristic pressure amplitude  $p_0$  on the surface of the array was calculated in three main anatomical planes of the head: sagittal ( $zx$ ), frontal ( $zy$ ), and axial ( $xy$ ); one-dimensional distributions  $p_A/p_0$  along the array axis were also found. To analyze the pressure levels reached near the surface of the skull, the pressure amplitude distributions  $p_A/p_0$  were calculated in a rectangular volume, the edges of which were distanced by 10 mm

from the surface of the skull, the upper edge was in water, and the lower one was in the brain. For the simulation, a computational grid with a spatial resolution of  $\Delta x = \Delta y = \Delta z = 0.5$  mm was used. Since the voxel size of the 3D acoustic head model was twice the grid resolution, each voxel was divided in half in each of the three directions. In this case, the type of medium for each voxel remained the same. The time resolution of the computational grid was chosen in accordance with the Courant–Friedrichs–Levy criterion and satisfied the condition  $CFL \equiv c_{\max} \Delta t / \Delta x$ , where  $CFL = 0.1$  and  $c_{\max}$  is the maximum sound speed in the model. To compensate for aberrations caused by skull bones, similar calculation methods were used, but in reverse order (Fig. 1f). First, the Kelvin–Voigt model (3) was used to simulate the propagation of a spherical wave from the focus to the  $xy$  plane near the skull. Next, the numerical solution of the Rayleigh integral (1) in a homogeneous medium was used to calculate the field in the  $xy$  plane and obtain the complex amplitudes and phases at the geometric center of each array element.

When calculating the field with aberration compensation, the obtained phases were inverted, while in calculations without compensation, the phase at each element was assumed to be zero. To achieve the maximum intensity at the focus, the amplitudes on the elements were set the same for all elements of the array [7]. For arrays with different numbers of elements and, accordingly, different active areas, the amplitude on their elements was chosen inversely proportional to the filling factor of the array, so that all transducers provided the same pressure amplitude at the focus when focusing in water. This normalization reveals the effect of the number of elements on the quality of aberration compensation “in its pure form.” Then, for the normalization constant  $p_0$  the characteristic initial pressure  $p_0 = c_0 \rho_0 v_0$  on the surface of the 256-element array was chosen.

Calculations were carried out for four arrays: 256-, 512-, 1024-element, and idealized array, at five different focusing depths with and without aberration compensation. The focal depth was changed by mechanically translating the array along its own axis and was 25, 35, 45, 55, and 65 mm (Fig. 1e, 1–5) from the inner surface of the skull. The center of the brain corresponds to a value of 55 mm (Fig. 1e, 4).

To estimate the relative contribution of different wave effects to the decrease of field intensity at the focus, additional calculations of the 256-element array field in water were performed. In the numerical model of focusing to the center of the brain without aberration compensation, different effects were sequentially turned off and the maximum attainable pressure amplitudes in the brain were compared in different approximations.

To assess the contribution of shear-wave generation in the skull, the sound speed  $c_s$  and absorption

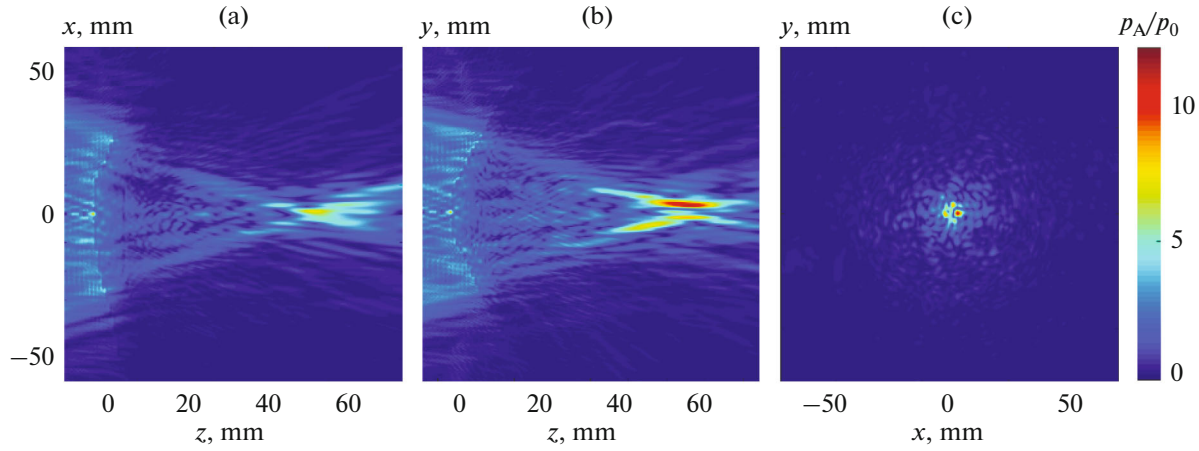


**Fig. 2.** Distribution of pressure amplitude  $p_A/p_0$  normalized to pressure amplitude  $p_0$  at array elements, in planes (a)  $xz$ , (b)  $zy$ , and (c)  $xy$  for insonation of center of brain using 256-element array without aberration compensation.

coefficient  $\alpha_s$  of shear waves in the matrix with acoustic parameters of the media were set equal to zero.

To estimate the contribution of longitudinal-wave absorption, each element of the 256-element array was connected to the focus, and for each absorbing medium (skin, bone, brain), the average distance  $\langle l^k \rangle = N^{-1} \sum_{i=1}^N l_i^k$  along the received rays was found. Here,  $N = 256$ ,  $k = \text{“s,“ “b,“ “br,“}$  which denote different media: “skin,” “skull bones,” and “brain tissue.” These distance values were used to estimate the decrease in pressure amplitude  $A$  due to absorption:

$$A = \exp(-\alpha_l^s \langle l^s \rangle - \alpha_l^b \langle l^b \rangle - \alpha_l^{br} \langle l^{br} \rangle). \quad (4)$$

Note that the contribution of absorption was estimated analytically, without numerical simulation, since switching off absorption in the pseudospectral numerical model led to multiple wave reflections in the skull.

The contribution of reflection was estimated in the plane-parallel layer approximation for normal incidence. Each medium retained its own impedance, but interfaces between different media were considered planar. Thus, the total pressure reflection coefficient  $R$  was calculated as the product of the reflection coefficients at the water–skin interface:  $R_{ws} = (\rho_s c_s - \rho_w c_w) / (\rho_s c_s + \rho_w c_w)$ , skin–skull  $R_{sb}$  and skull–brain  $R_{bbr}$  interfaces:

$$R = R_{ws} R_{sb} R_{bbr}. \quad (5)$$

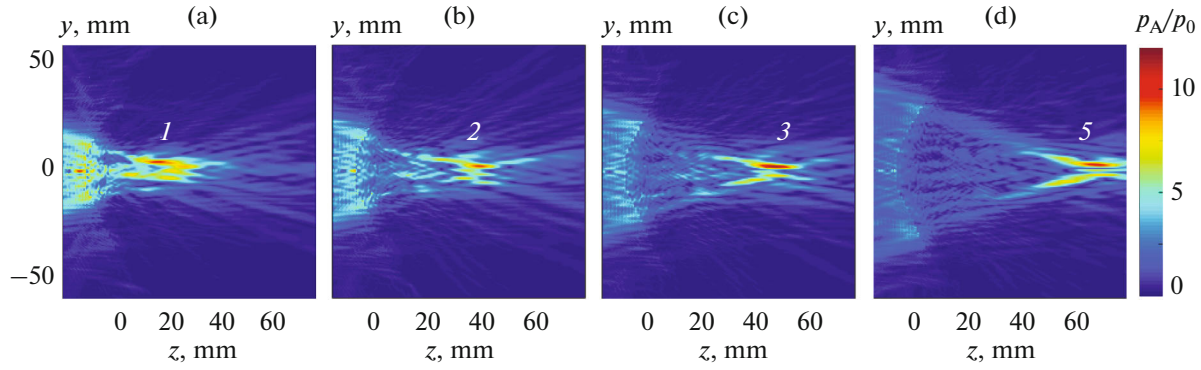
The effect of aberrations was estimated taking into account the results obtained for shear waves, absorption, and reflection, which weaken the field in the focal region of the beam. For this, the maximum pressure achieved during focusing to the center of the brain without aberration compensation  $p_A/p_0$  was divided by pressure amplitudes weakened due to shear-wave generation, absorption, and reflection. The ratio of the obtained pressure amplitude and maximum pressure

in water was taken as the contribution of aberrations to the beam distortion.

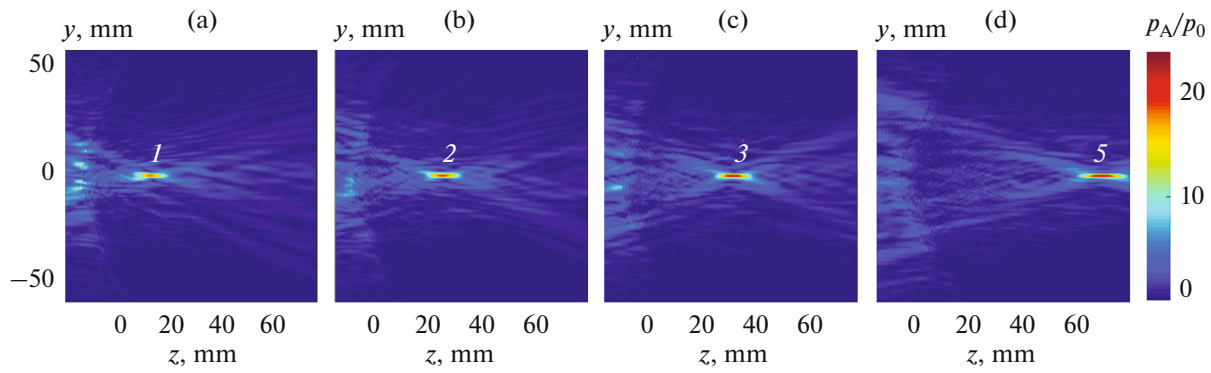
## RESULTS

Figure 2 shows two-dimensional distributions of the dimensionless pressure amplitude  $p_A/p_0$  normalized to the initial characteristic value  $p_0$  on the surface of the 256-element array, when the center of the brain is irradiated without aberration compensation (Fig. 1e, 4). The value  $z = 0$  corresponds to the inner surface of the skull. The results are presented in three main anatomical planes passing through the center of curvature of the array: sagittal, dividing the head into right and left halves ( $zx$ ); frontal, to the front and back halves ( $zy$ ); and axial, to the upper and lower halves ( $xy$ ). In the absence of phase correction, the acoustic field is strongly distorted by skull bones, the maximum pressure is displaced relative to the center of curvature of the transducer, and  $p_A/p_0 = 12.5$ , whereas for focusing in water, the pressure gain at the focus is 100. Additional pressure maxima near the skull and blurring of the focus are also observed.

Figure 3 shows the effect of aberrations at different focusing depths. To change the focusing depth, the transducer was mechanically displaced downward along its own axis by  $-10$  mm, and upward by  $+10$ ,  $+20$ , and  $+30$  mm relative to the center of the brain (Fig. 1e, 5, 3, 2, 1). The calculation results are shown in the form of two-dimensional distributions of  $p_A/p_0$  in the  $zy$  plane. For all focus position depths, strong distortions of the ultrasound beam, blurring of the focal region, and additional pressure maxima near the skull are present. As the depth of focus decreases, these effects become more pronounced. At greater focusing depths,  $-10$  and  $+10$  mm relative to the center of the brain (Figs. 3c, 3d), the pressure amplitude near the skull is 60–70% of the maximum value  $p_A/p_0$ .



**Fig. 3.** Distribution of normalized pressure amplitude  $p_A/p_0$  in  $zy$  plane for focusing in brain at different depths without aberration compensation for 256-element array. Array center of curvature was shifted relative to center of brain by (a)  $-30$ , (b)  $-20$ , (c)  $-10$ , (d)  $+10$  mm.



**Fig. 4.** Distribution of normalized pressure amplitude  $p_A/p_0$  in  $zy$  plane for focusing at different depths in brain with aberration compensation for 256-element array. Array center of curvature was shifted relative to the center of brain by (a)  $-30$ , (b)  $-20$ , (c)  $-10$ , (d)  $+10$  mm.

For focusing and irradiation of the brain closer to the skull, at a depth of 35–25 mm from its inner surface (Figs. 3a and 3b), the pressure amplitude near the skull becomes comparable to that at the focus. The maximum pressure and intensity in the brain in case of the most shallow focusing position (Fig. 3a) decreases by 1.3 dB (14 and 26%, respectively) versus irradiation of the center of the brain. Thus, a decrease in the focal depth and irradiation of structures close to the inner surface of the skull increases the distortion of the ultrasound beam, decreases the pressure amplitude at the focus, and increases it near the skull bone.

The quality of aberration correction at different focusing depths is illustrated in Fig. 4, which shows two-dimensional amplitude distributions of the dimensionless acoustic pressure  $p_A/p_0$  in the  $zy$  plane. Aberration compensation was performed for the 256-element array for irradiation at the same depths as in Fig. 3. As clearly seen, the correction significantly improves the focusing quality, namely, restores the focus position, provides a narrow beam waist at the focus, and increases the pressure amplitude almost by a factor of 2. For irradiation of the center of the brain,

the pressure at the focus is  $p_F/p_0 = 23.8$ . On the one-dimensional distributions along the array axis (Fig. 5), one can see in more detail the result of correction at different depths. The width and length of the focal lobe at all focusing depths are practically the same as in the case of focusing in water and are, respectively, about 2 and 14 mm at half-maximum of the focal peak. However, with decreasing focusing depth, when the array is raised by 30 mm relative to the center of the brain (Fig. 4a), there is a decrease in pressure and intensity at the focus by 1.6 dB (17 and 30%, respectively). As the focus is shifted towards the surface of the skull, the level of the side pressure maxima near the skull also increases from 40% (for irradiation of the center of the brain) to 76% (in the most shallow position) of  $p_F/p_0$ . This corresponds to 16 and 58% in terms of the intensity level, respectively.

Figure 6 shows the effect of the number of elements on the efficiency of aberration compensation. The dependence of  $p_A/p_0$  on the focusing depth measured from the inner surface of the skull is plotted for the 256-, 512-, 1024-element and idealized arrays (Figs. 1a–1d). The upper part of the plot shows the

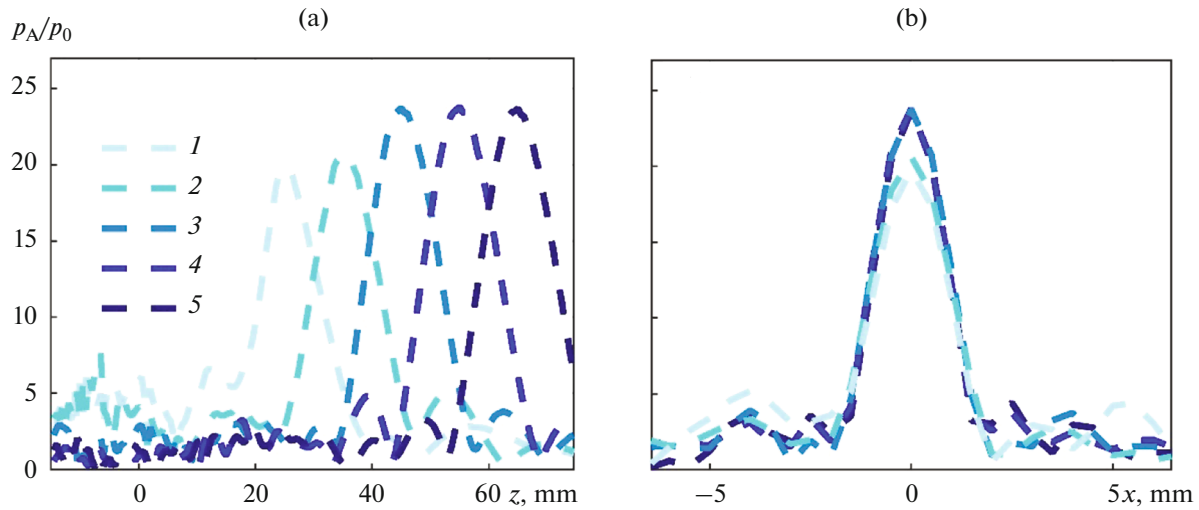


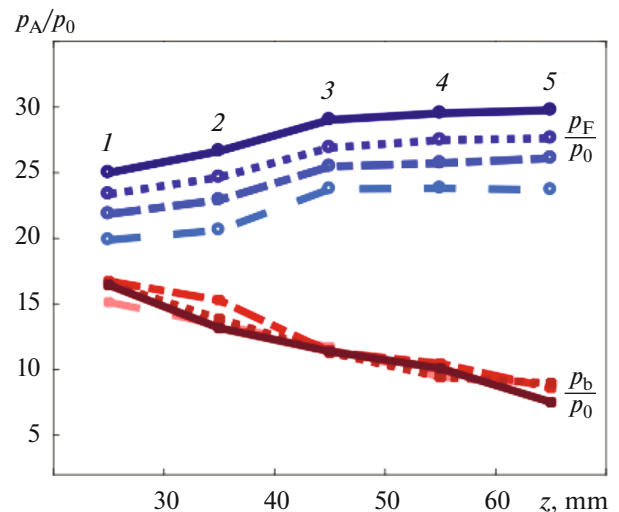
**Fig. 5.** Distribution of normalized pressure amplitude  $p_A/p_0$  (a) along array axis and (b) in focal plane for focusing at different depths in brain with aberration compensation for 256-element array. Array center of curvature was shifted relative to the center of brain by  $-30$  (1),  $-20$  (2),  $-10$  (3),  $0$  (4),  $+10$  mm (5).

normalized pressure amplitude at the focus of the transducer  $p_F/p_0$  for the idealized (solid line), 1024-element (dotted line), 512-element (dash-dotted line), and 256-element (dashed line) arrays. The curves at the bottom of the plot are the maximum pressure values near the surface of the skull bone  $p_b/p_0$ . Numerals 1-5 correspond to the focusing depths noted in Fig. 1d. Recall that the  $p_A$  values here are normalized to the characteristic value  $p_0$  on the surface of the 256-element array, so that all arrays yield the same pressure amplitude at the focus when focusing in water.

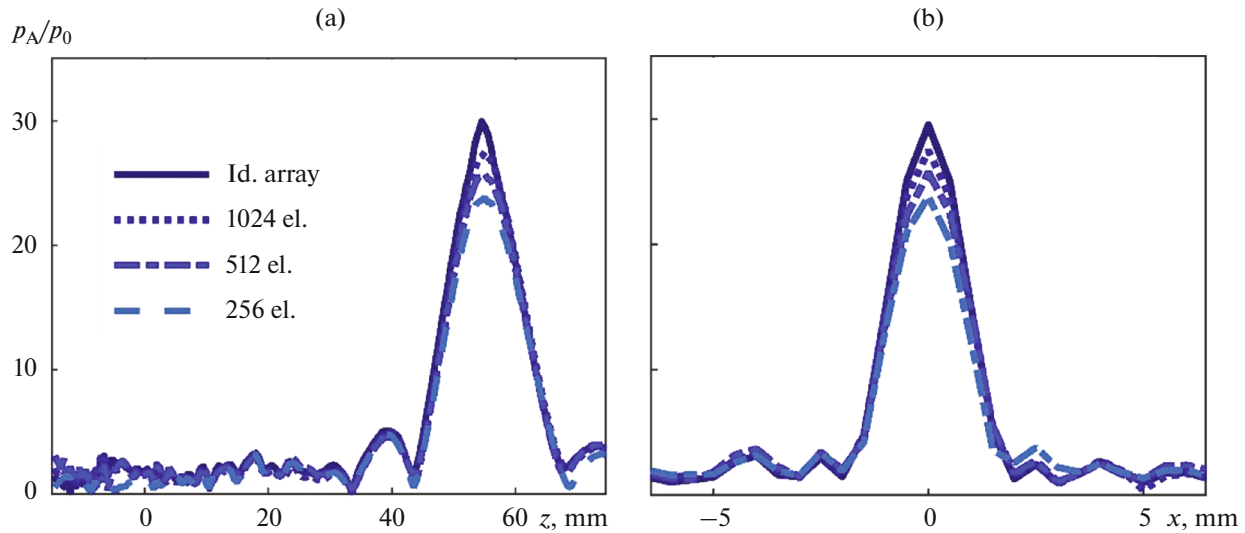
The plot illustrates that with an increased number of transducer elements, the pressure amplitude at the focus increases. Thus, for an idealized array, the pressure and intensity increase by 1.9 dB (by 24 and 55%, respectively) versus the 256-element array, and by 0.62 dB (by 7 and 15%, respectively) versus the 1024-element array. When passing from 256 to 512 elements, the increase in pressure and intensity at the focus is 0.67 dB (8 and 17%); when passing from 512 to 1024 elements, 0.57 dB (7 and 14%). With a decrease in focusing depth, the pressure amplitude at the focus decreases approximately the same for all transducers: the pressure amplitude at the shallow focus depth positions (1 and 5 in Fig. 6) differ by 17%. The maximum pressure levels near the surface of the skull change insignificantly with an increased number of elements. In this case, the pressure amplitude near the skull increases by a factor of 1.68 with a decrease in focusing depth in the considered interval (positions 1 and 5).

Figure 7 compares the shape of the focal peak and attainable pressure levels for arrays with different numbers of elements. One-dimensional normalized pressure amplitude distributions  $p_A/p_0$  are plotted

along the array axis  $z$  and along the axis  $x$  in the focal plane for focusing in the center of the brain for arrays with different numbers of elements and for the idealized array. The value  $z = 0$  corresponds to the inner surface of the skull. It can be seen from the distributions that the structure of the field and the longitudinal and transverse dimensions of the focal region of all transducers, determined from the half-maximum and the first zeros of pressure with respect to the maximum pressure, are nearly the same for all arrays. However,



**Fig. 6.** Values of normalized pressure amplitude at focus  $p_F/p_0$  and maximum pressure amplitude near surface of skull bone  $p_b/p_0$  for arrays with 1024 (dotted line), 512 (dash-dotted line), and 256 elements (dashed line) and idealized array (solid line) for focusing at different depths: 25 (1), 35 (2), 45 (3), 55 (thalamus region, 4), 65 mm (5) from inner surface of skull.



**Fig. 7.** Distribution of normalized pressure amplitude  $p_A/p_0$  (a) along array axis and (b) in focal plane for different arrays: 256 (dashed line), 512 (dash-dotted line), and 1024 elements (dotted line) and idealized case (solid line) in case of insonation of center of brain with aberration compensation.

an increase in the number of array elements makes it possible to increase the absolute pressure level at the focus of the transducer.

A stage-by-stage analysis of the influence of different wave effects on a decrease in the maximum attainable pressure levels in the focal region yielded the following results. At the first step, when shear-wave generation was turned off, the maximum of the field pressure amplitude increased by 2 dB, while the displacement relative to the geometric focus of the array, sidelobe maxima, and blurring of the focus remained the same. Additional switching off the absorption led to an increase in the pressure amplitude by 6.7 dB. When reflection was turned off, the pressure maximum increased by another 2.1 dB, and with the subsequent aberration compensation—by 7.4 dB. Thus, our estimates show that the greatest contribution to the beam attenuation comes from aberrations; absorption adds somewhat smaller, but comparable contribution. The effects of reflection and shear wave generation in the skull on the beam propagation are less significant.

## CONCLUSIONS

The study analyzes the possibilities of correcting aberrations at different focusing depths in brain structures for the proposed new type of arrays with different numbers of elements. It is shown that with transcranial insonation of brain structures with the proposed arrays, aberration compensation can significantly improve the focusing quality and achieve a narrow focal lobe with a width and length of about 2 and 14 mm at half-maximum of the focal peak in the depth range from 25 to 65 mm from the inner surface of the skull. The width and length of the focal lobe nearly

coincide with those for focusing in water. Thus, the possibility of changing the focusing depth inside the brain within 4 cm by mechanical movement of the array in the axial direction was demonstrated. With a decrease in focusing depth, the quality of aberration correction somewhat deteriorates. For example, with the 256-element array, for the shallowest focus position (25 mm depth), the pressure amplitude at the focus is 91% of the deepest focusing (65 mm). The level of pressure maxima near the skull increases by 1.68 times, mainly because the skull bones get closer to the high-intensity focal region in the converging ultrasound beam. This effect is not associated with the presence of the skull on the beam path. Auxiliary calculations show that if all heterogeneities are excluded from the acoustic model and only water remains as the propagation medium, then calculations yield the same pressure levels near the proposed location of the skull.

Focusing in the mentioned depth interval was analyzed for different numbers of array elements: 256, 512, 1024, as well as for the idealized case of quasi-continuous phase change over the transducer surface. For all arrays, with a decrease in focusing depth, the same pattern of decrease in pressure level at the focus is observed: it decreases by approximately the same percentage with the change in depth. As well, the level of pressure maxima near the skull is practically independent on the number of radiating elements, which is quite consistent with the above suggestion that this effect is actually determined only by the focusing geometry of the field. Increasing the number of elements also increases the pressure amplitude at the transducer focus. The largest increase by 8% (at 0.67 dB) is observed when passing from 256 to 512 elements. An increase in the number of elements above 1024 seems

is less advantageous, since the increase in pressure amplitude when passing from 1024 elements to the idealized array is only 7%, which is even less than when passing from 256 to 512 elements.

When assessing the influence of various effects on the focusing quality, it was shown that the greatest contribution to the beam attenuation comes from aberrations, reducing the maximum attainable pressure amplitude by 7.4 dB; absorption introduces 6.7 dB of losses, 2.1 dB losses are introduced by reflection, and 2 dB - by shear-wave generation. This result clearly demonstrates the importance of further developing aberration correction algorithms as the way to suppress the most significant source of weakening the ultrasound field parameters at the focus.

Despite the fact that all calculations in this study were carried out with linear acoustic models, it is of practical interest to apply the aberration correction results not only for thermal ablation with harmonic waves, but also for boiling histotripsy based on mechanical tissue destruction at the focus using nonlinear shock waves. Such an approach is reasonable, since it was previously shown that the phases on array elements calculated in the linear approximation compensate for aberrations when nonlinear effects are also taken into account [12]. In addition, the nonlinear distortions accumulating with distance in the wave profile and the formation of shock fronts, which are necessary to generate mechanical damages, are less developed near the surface of the skull than at the focus, which means they would not have destructive capabilities even at relatively high pressures. To quantitatively account for nonlinear effects when determining the safe area of action for the proposed arrays, calculations should be done using more complex numerical models [27, 28]. Note also that this study analyzed the possibilities of aberration correction using mechanical movement of the array. Subjects for further research are generalization of the proposed model to the case of electronic steering of the focus along and across the array axis and analysis of how inhomogeneities in the internal structure of skull bones affect the distortion of the ultrasound beam.

In conclusion, the paper considers the possibility of correcting aberrations at different focusing depths in brain structures for the proposed arrays with different numbers of elements. They differ from the existing arrays used in clinical practice by higher frequency, randomized arrangement of elements, which makes it possible to reduce the level of the array sidelobes, fully populated filling of the array with elements, and, perhaps most importantly, the compact shape and relatively small convergence angle, which makes it possible to rotate and relocate them relative to a patient's head without significant changing the angle of incidence of the HIFU beam on the skull. Therefore, the proposed arrays can potentially extend the range of axial steering of the array focus compared to hemi-

spherical arrays used in clinical practice, which have a more restrictive range of motion to mechanically steer the focus. This gives a potential for possible enlargement of the spatial area of effective and safe HIFU insonation of brain structures through an intact skull.

#### FUNDING

The study was carried out within the frame of the Interdisciplinary Scientific and Educational School of Moscow State University "Photonic and Quantum Technologies: Digital Medicine" and support from the Russian Foundation for Basic Research (project no. 19-02-00035).

#### CONFLICT OF INTEREST

The authors declare that they have no conflicts of interest.

#### REFERENCES

1. W. Qiu, A. Bouakaz, E. Konofagou, and H. Zheng, *IEEE Trans. Ultrason., Ferroelectr. Freq. Control* **68** (1), 6 (2020).
2. N. McDannold, G. Clement, P. Black, F. Jolesz, and K. Hynynen, *Neurosurgery* **66** (2), 323 (2010).
3. D. Jeanmonod, B. Werner, A. Morel, L. Michels, E. Zadicario, G. Schiff, and E. Martin, *Neurosurg. Focus* **32** (1), E1 (2012).
4. W. J. Elias, D. Huss, T. Voss, J. Loomba, M. Khaled, E. Zadicario, R. C. Frynsinger, S. A. Sperling, S. Wylie, S. J. Monteith, J. Druzgalm, B. B. Shahm, M. Harrison, and M. Wintermark, *N. Engl. J. Med.* **369** (7), 640 (2013).
5. W. J. Elias, *N. Engl. J. Med.* **375** (8), 730 (2016).
6. S. Monteith, R. Medel, N. F. Kassell, W. Wintermark, M. Eames, J. Snell, E. Zadicario, J. Grinfeld, J. P. Sheehan, and W. J. Elias, *J. Neurosurg.* **118** (2), 319 (2013).
7. L. R. Gavrilov, *Focused High Intensive Ultrasound in Medicine* (Fazis, Moscow, 2013) [in Russian].
8. K. Hynynen and R. M. Jones, *Phys. Med. Biol.* **61**, 206 (2016).
9. J. Sun and K. Hynynen, *J. Acoust. Soc. Am.* **104** (3), 1705 (1998).
10. M. Pernot, J.-F. Aubry, M. Tanter, J.-L. Thomas, and M. Fink, *Phys. Med. Biol.* **48** (16), 2577 (2003).
11. G. T. Clement and K. Hynynen, *Phys. Med. Biol.* **47** (8), 1219 (2002).
12. P. B. Rosnitskiy, P. V. Yuldashev, O. A. Sapozhnikov, L. R. Gavrilov, and V. A. Khokhlova, *J. Acoust. Soc. Am.* **146** (3), 1786 (2019).
13. P. B. Rosnitskiy, L. R. Gavrilov, P. V. Yuldashev, O. A. Sapozhnikov, and V. A. Khokhlova, *Acoust. Phys.* **63** (5), 531 (2017).
14. P. B. Rosnitskiy, B. A. Vysokanov, L. R. Gavrilov, O. A. Sapozhnikov, and V. A. Khokhlova, *IEEE Trans. Ultrason., Ferroelectr. Freq. Control* **65** (4), 630 (2018).
15. B. I. Raju, C. S. Hall, and R. Seip, *IEEE Trans. Ultrason., Ferroelectr. Freq. Control* **58** (5), 944 (2011).

16. P. Ramaekers, M. Ries, C. T. W. Moonen, and M. de Greef, *Med. Phys.* **44** (3), 1071 (2017).
17. T. D. Khokhlova, M. S. Canney, V. A. Khokhlova, O. A. Sapozhnikov, L. A. Crum, and M. R. Bailey, *J. Acoust. Soc. Am.* **130** (5), 3498 (2011).
18. V. A. Khokhlova, J. B. Fowlkes, W. W. Roberts, G. R. Schade, Z. Xu, T. D. Khokhlova, T. L. Hall, A. D. Maxwell, Y. N. Wang, and C. A. Cain, *Int. J. Hypertermia* **31** (2), 145 (2015).
19. A. Maxwell, O. Sapozhnikov, M. Bailey, L. Crum, Z. Xu, B. Fowlkes, C. Cain, and V. Khokhlova, *Acoust. Today* **8**, 24 (2012).
20. S. A. Ilyin, P. V. Yuldashev, V. A. Khokhlova, L. R. Gavrilov, P. B. Rosnitskiy, and O. A. Sapozhnikov, *Acoust. Phys.* **61** (1), 52 (2015).
21. S. Bobkova, L. Gavrilov, V. Khokhlova, A. Shaw, and J. Hand, *Ultrasound Med. Biol.* **36** (6), 888 (2010).
22. B. E. Treeby and B. T. Cox, *J. Acoust. Soc. Am.* **136** (4), 1499 (2014).
23. B. E. Treeby, J. Jaros, D. Rohrbach, and B. T. Cox, in *Proc. IEEE Int. Ultrasonics Symp.* (Chicago, 2014), p. 146.
24. F. A. Duck, *Physical Properties of Tissue: a Comprehensive Reference Book* (Acad. Press, London, 1990).
25. P. J. White, G. T. Clement, and K. Hynynen, *Ultrasound Med. Biol.* **32** (7), 1085 (2006).
26. H. T. O'Neil, *J. Acoust. Soc. Am.* **21** (5), 516 (1949).
27. P. V. Yuldashev and V. A. Khokhlova, *Acoust. Phys.* **57** (3), 334 (2011).
28. P. B. Rosnitskiy, P. V. Yuldashev, O. A. Sapozhnikov, A. D. Maxwell, W. Kreider, M. R. Bailey, and V. A. Khokhlova, *IEEE Trans. Ultrason., Ferroelectr. Freq. Control* **64** (2), 374 (2017).